JACS
JOURNAL OF THE AMERICAN CHEMICAL SOCIETY
Article
Cite This: J. Am. Chem. Soc. 2017, 139, 15691-15700
pubs.acs.org/JACS

A Terminal Iron(IV) Nitride Supported by a Super Bulky Guanidinate Ligand and Examination of Its Electronic Structure and Reactivity

Arnab K. Maity,[†] Jesse Murillo,[†] Alejandro J. Metta-Magaña,[†] Balazs Pinter,*[,‡] and Skye Fortier*[,†]

[†]Department of Chemistry, University of Texas at El Paso, El Paso, Texas 79968, United States

[‡]Computational OrganoMetallic and Inorganic Chemistry Group, Eenheid Algemene Chemie, Vrije Universiteit Brussel, Pleinlaan 2, Brussels 1050, Belgium

Supporting Information

ABSTRACT: Utilizing the bulky guanidinate ligand $[L^{Ar*}]^-$ (L^{Ar*} = $(Ar*N)_2C(R)$, Ar* = 2,6-bis(diphenylmethyl)-4-*tert*-butylphenyl, R = NC^tBu_2) for kinetic stabilization, the synthesis of a rare terminal Fe(IV) nitride complex is reported. UV irradiation of a pyridine solution of the Fe(II) azide $[L^{Ar*}]FeN_3(py)$ (**3-py**) at 0 °C cleanly generates the Fe(IV) nitride $[L^{Ar*}]FeN(py)$ (**1**). The ^{15}N NMR spectrum of the $\mathbf{1}^{15N}$ (50% Fe≡^{15}N) isotopomer shows a resonance at 1016 ppm (vs externally referenced CH_3NO_2 at 380 ppm), comparable to that known for other terminal iron nitrides. Notably, the computed structure of **1** reveals an iron center with distorted tetrahedral geometry, τ_4 = 0.72, featuring a short Fe≡N bond (1.52 Å). Inspection of the frontier orbital ordering of **1** shows a relatively small HOMO/LUMO gap with the LUMO comprised by Fe($d_{xz,yz}$)N($p_{x,y}$) π*-orbitals, a splitting that is manifested in the electronic absorption spectrum of **1** (λ = 610 nm, ε = 1375 L·mol^{-1}·cm^{-1}; λ = 613 nm (calcd)). Complex **1** persists in low-temperature solutions of pyridine but becomes unstable at room temperature, gradually converting to the Fe(II) hydrazide product $[\kappa^2$-($^tBu_2CN$)C(η^6-NAr*)(*N*-NAr*)]Fe (**4**) upon standing via intramolecular N-atom insertion. This reactivity of the Fe≡N moiety was assessed through molecular orbital analysis, which suggests electrophilic character at the nitride functionality. Accordingly, treatment of **1** with the nucleophiles PMe_2Ph and Ar−N≡C (Ar = 2,6-dimethylphenyl) leads to partial N-atom transfer and formation of the Fe(II) addition products $[L^{Ar*}]Fe(N{=}PMe_2Ph)(py)$ (**5**) and $[L^{Ar*}]Fe(N{=}C{=}NAr)(py)$ (**6**). Similarly, **1** reacts with $PhSiH_3$ to give $[L^{Ar*}]Fe[N(H)(SiH_2Ph)](py)$ (**7**) which Fukui analysis shows to proceed via electrophilic insertion of the nitride into the Si−H bond.

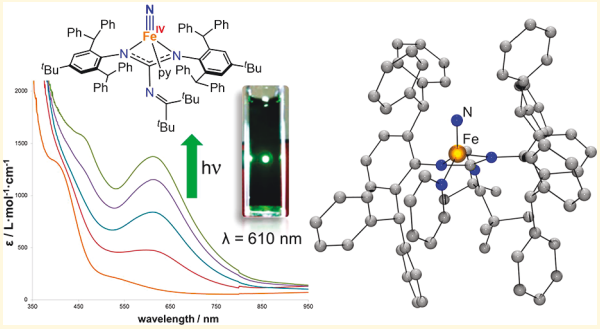

INTRODUCTION

In the Haber−Bosch process, iron nitride species have been detected in the conversion of N_2 to NH_3,[1] while mononuclear iron nitrides, such as $[Fe^{IV}]{\equiv}N$, have been invoked as possible intermediates in the fixation of N_2 by nitrogenase.[2] Accordingly, the chemistry of iron nitride complexes has been an area of intense interest.[2d,e] However, in many respects, investigations have been hampered by the paucity of mononuclear model complexes featuring terminal Fe≡N bonds. Whereas dozens of molecular complexes with terminal Fe=O functionalities have now been synthesized and studied,[3] only a handful of Fe≡N complexes have been isolated or spectroscopically detected.[2d,e] As a consequence, much remains to be learned about the electronic and structural factors which affect the chemistry of the Fe≡N motif.

In 2004, Peters and co-workers reported the synthesis of $[PhB(CH_2P^iPr_2)_3]Fe^{IV}{\equiv}N$ (**A**, Chart 1), the first room temperature persistent iron compound with a terminating nitride ligand.[4] This complex is only isolable in solution as dimerization occurs through bimolecular N-atom coupling to give $\{[PhB(CH_2P^iPr_2)_3]Fe^{I}\}(\mu\text{-}N_2)$ upon drying. Nonetheless, **A** is sufficiently stable to allow detailed spectroscopic measurements including XAS which revealed the presence of a short Fe≡N bond (ca. 1.52 Å) consistent with highly covalent, triple bond

Chart 1. Isolable Terminal Fe(IV) Nitrides

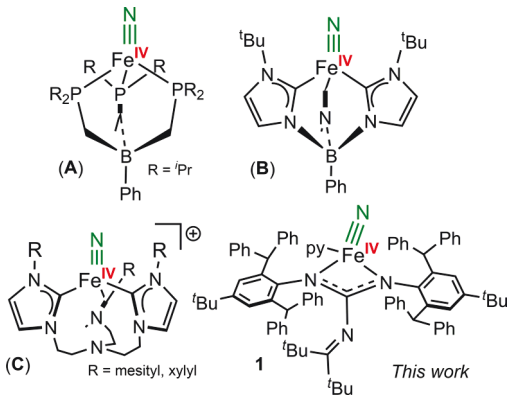

Received: July 3, 2017
Published: September 27, 2017

DOI: 10.1021/jacs.7b06919
J. Am. Chem. Soc. 2017, 139, 15691−15700

character.[5] Subsequently in 2008, the groups of Smith and Meyer, independently, reported the respective isolation of $[PhB(^{tBu}Im)_3]Fe^{IV}{\equiv}N$ (**B**) and $[(TIMEN^{R})Fe^{IV}{\equiv}N]^+$ (**C**) in the solid-state as thermally stable compounds (Chart 1).[6] X-ray crystallographic analyses and DFT calculations for **B** and **C** show similarly short Fe≡N triple bonds (1.512(1) Å (**B**); 1.526(2)−1.527(3) Å (**C**)) with substantial iron−nitrogen orbital overlap. In all three cases, each possesses four-coordinate, pseudotetrahedral iron ligated by strongly σ-donating (weakly π-accepting) tripodal phosphine or NHC groups, thus situating the metal within a strong-field ligand environment.

Conspicuously, compounds with terminal Fe≡N units supported by hard donor, weak-field ligands have yet to be isolated. This is not altogether surprising as weak ligand fields produce smaller d-orbital splittings that favor high-spin configurations. Consequently, Fe≡N antibonding orbitals can become populated leading to unstable Fe−N bonds that are prone to bridging or other reactivity. For instance, Holland recently described the reduction chemistry of the iron β-diketiminate $[LFeCl]_2$ (L = $MeC[C(Me)N(2,6\text{-}Me_2C_6H_3)]_2^-$) which reductively cleaves N_2 to give a tetrairon product with two bridging nitride ligands.[7] Yet, the role of molecular geometry cannot be understated as it too plays a significant part in the stability of iron nitride compounds. Seminal studies by Wieghardt and others demonstrated that six-coordinate, octahedral iron nitrides of the type $[(\kappa^5\text{-cyclamAc})FeN]^{n+}$ and nominally five-coordinate nitrides such as (porphyrin)FeN are photochemically accessible at low temperatures (≤80 K) in frozen MeCN matrices but are unstable upon warming.[8] In the case of $[(\kappa^5\text{-cyclamAc})Fe^{V}N]^+$, as a consequence of its octahedral geometry, the orbital ordering leads to partial occupancy of a $Fe(d_{xz,yz})N(p)$ π^*-orbital,[8c] thus weakening the Fe−N bond and thereby diminishing its stability. In the absence of isolable, four-coordinate iron nitrides in weak ligand fields that are comparable in geometric form to **A**−**C**, it is difficult to assess the role that ligand field strength plays versus coordination environment in the stability and reactivity of the Fe≡N functionality.

Recently, we described the synthesis and full structural characterization of the super bulky guanidinate ligand $[L^{Ar*}]^-$ (L^{Ar*} = $(Ar*N)_2C(R)$, Ar* = 2,6-bis(diphenylmethyl)-4-*tert*-butylphenyl, R = NC^tBu_2), which is capable of supporting formally low-coordinate alkali metals within a sterically protected ligand pocket.[9] We reasoned that $[L^{Ar*}]^-$, as a weak field ligand, would provide a highly suitable framework for the synthesis of iron nitride complexes as (a) the sterically encumbering ligand architecture would provide the kinetic stabilization necessary to protect reactive Fe≡N bonds and prevent Fe−N−Fe bridging, and (b) the donor properties of the guanidinate would be sufficient to support the high oxidation states needed to access and favor Fe≡N formation. Successfully, we herein report the synthesis of the Fe(IV) nitride complex $[L^{Ar*}]FeN(py)$ (py = NC_5H_5) (**1**, Chart 1) that is generated photochemically and is stable in solution at ∼273 K for several hours. Complex **1** has been characterized by electronic absorption and NMR spectroscopies, including ^{15}N NMR spectroscopic analysis of isotopically enriched $\mathbf{1}^{15N}$ (50% $Fe{\equiv}^{15}N$). Additionally, its electronic structure has been modeled through computational analysis, revealing Fe≡N bonding that is distinct from **A**−**C**. Finally, the reactivity of the nitride unit in **1**, manifested through partial N-atom transfer to nucleophilic type substrates, is described.

RESULTS AND DISCUSSION

Synthesis and Characterization. Addition of $K[L^{Ar*}]$ to $FeCl_2$ in THF affords the Fe(II) complex $[L^{Ar*}]FeCl(THF)$ (**2**) in 76% yield as a highly crystalline, colorless solid that can be produced on a multigram scale. The ^1H NMR spectrum of **2** in C_6D_6 shows resonances which occur from 22.7 to −17.5 ppm. While the *tert*-butyl protons of the aniline and ketimine substituents appear as two prominent resonances at 22.7 and −1.5 ppm, the anticipated peak set for **2** is lacking several resonances, a likely consequence of significant paramagnetic broadening. Consistent with this, the solution magnetic moment of **2** (μ_{eff} = 5.1 μ_B (Evans method)) at room temperature in py-d_5 indicates a high-spin Fe(II), S = 2, center. Complex **2** is soluble in THF and aromatic solvents but only partially soluble in Et_2O and nonpolar solvents such as hexanes. Single crystals of **2** suitable for X-ray crystallographic analysis were harvested from a saturated Et_2O solution stored at −30 °C for 2 days. The solid-state structure of **2**·Et_2O (Figure 1) reveals a four-coordinate iron

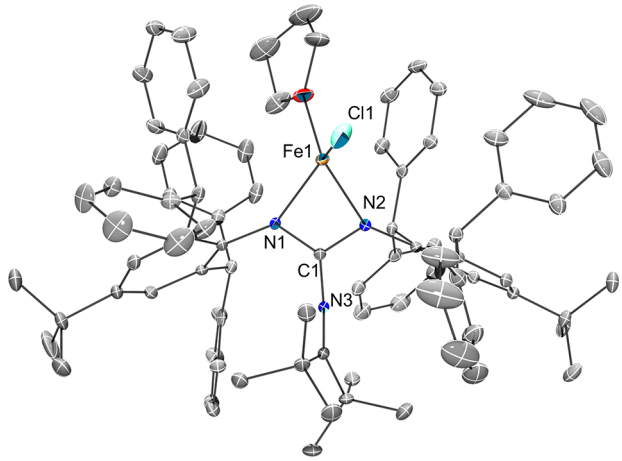

Figure 1. ORTEP diagram of **2**·Et_2O with 30% thermal probability ellipsoids. Hydrogen atoms and co-crystallized Et_2O are omitted for clarity. Selected bond lengths (Å) and angles (deg): Fe1−N1 = 2.042(9), Fe1−N2 = 2.098(1), Fe1−Cl1 = 2.244(4), N1−Fe1−N2 = 65.21(6), N1−Fe1−Cl1 = 113.42(5).

with distorted tetrahedral geometry. Complex **2**·Et_2O is monomeric, a rare feature given that most bulky $[R'C(NR)_2]^-$ and β-diketiminate iron(II) halides are found as diamond bridged dimers,[10] signaling that the $[L^{Ar*}]^-$ ligand is sufficiently encumbering to impede the formation of single-atom bridged species.

Treatment of **2** with excess NaN_3 in THF yields the dinuclear bis(azide) ferrate(II) complex $[[Na(Et_2O)_2]\{[L^{Ar*}]Fe(N_3)_2\}]_2$ (**3-NaN$_3$**) as a colorless solid in 90% yield. The extra coordinated equivalent of NaN_3 is readily removed by addition of a few drops of pyridine to a toluene solution of **3-NaN$_3$** to give the neutral complex $[L^{Ar*}]Fe(N_3)(py)$ (**3-py**). The ^1H NMR spectra of **3-NaN$_3$** and **3-py** are qualitatively very similar to that of **1** as they feature paramagnetically broadened resonances across a wide chemical shift range. As with **1**, the solution magnetic moment as determined by Evans method for **3-py** in py-d_5 (25 °C) is found to be μ_{eff} = 5.2 μ_B, in accordance with high-spin Fe(II). Both **3-NaN$_3$** and **3-py** are sparingly soluble in nonpolar solvents and Et_2O but fully soluble in THF. Single crystals of **3-NaN$_3$** were grown from a solution of THF/Et_2O stored at −30 °C, while crystals of **3-py**·C_6H_6 were harvested from a

DOI: 10.1021/jacs.7b06919
J. Am. Chem. Soc. 2017, 139, 15691−15700

concentrated benzene solution stored at room temperature. The solid-state structures of **3-NaN$_3$** (Figure S1) and **3-py**·C$_6$H$_6$ (Figure 2) retain a distorted tetrahedral coordination environment about the iron.

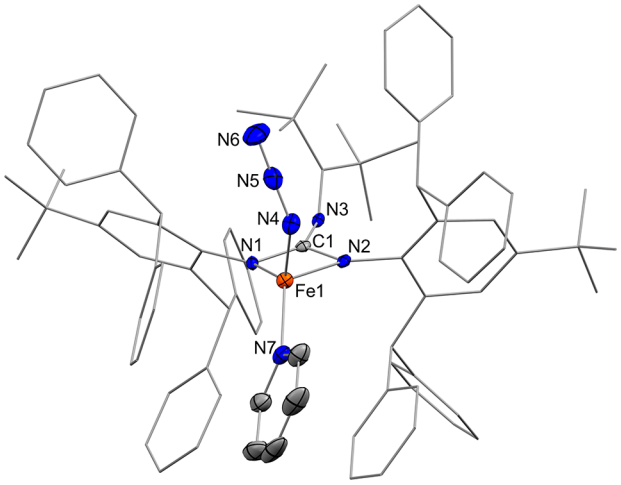

Figure 2. ORTEP diagram of **3-py**·C$_6$H$_6$ with 30% thermal probability ellipsoids. Hydrogen atoms and co-crystallized molecule of C$_6$H$_6$ are omitted for clarity. Peripheral bonds de-emphasized for simplicity. Selected bond lengths (Å) and angles (deg): Fe1–N4 = 1.966(4), N4–N5 = 1.202(5), N5–N6 = 1.158(5), Fe1–N4–N5 = 138.7(3), N7–Fe1–N4 = 103.6(8).

The Fe–N$_\alpha$, N$_\alpha$–N$_\beta$, and N$_\beta$–N$_\gamma$ bond lengths and Fe–N$_\alpha$–N$_\beta$ angles of the azide units in **3-NaN$_3$** (Fe–N$_\alpha$ = 1.935(2) Å; Fe–N$_\alpha$–N$_\beta$ = 165.7(2)°; N$_\alpha$–N$_\beta$ = 1.176(3) Å; N$_\beta$–N$_\gamma$ = 1.162(3) Å) and **3-py**·C$_6$H$_6$ (Fe–N$_\alpha$ = 1.966(4) Å; Fe–N$_\alpha$–N$_\beta$ = 138.7(3)°; N$_\alpha$–N$_\beta$ = 1.202(5) Å; N$_\beta$–N$_\gamma$ = 1.158(5) Å) are ordinary and are comparable to the values found for four-coordinate iron in [(TIMEN^R)Fe(N$_3$)]$^+$ (e.g., Fe–N$_\alpha$ = 1.955(2) Å; Fe–N$_\alpha$–N$_\beta$ = 166.9(2)°) and (PNP)Fe(N$_3$) (e.g., Fe–N$_\alpha$ = 1.961(1) Å; Fe–N$_\alpha$–N$_\beta$ = 137.5(1)°).[6c,11] The Fe–N$_3$ azide stretch of **3-NaN$_3$** (ν_{N_3} = 2077 cm^{-1}) and **3-py** (ν_{N_3} = 2073 cm^{-1}) is similar to that of [PhB($^{t\mathrm{Bu}}$Im)$_3$]Fe(N$_3$) (ν_{N_3} = 2081 cm^{-1}).[6a] Altogether, these parameters indicate little activation of the N$_3^-$ unit and signify predominantly ionic character in the Fe–N$_3$ bond.[12]

Complexes **3-NaN$_3$** and **3-py** are thermally stable solids and show no sign of change when heated under vacuum at 100 °C for several hours. Similarly, prolonged exposure of these solids to UV-irradiation under vacuum causes a slight darkening of the material with no detectable change in their NMR spectra. On the other hand, **3-NaN$_3$** and **3-py** are sensitive to UV-light in solution. Photolysis of C$_6$D$_6$ solutions of **3-NaN$_3$** and **3-py** at room-temperature results in a significant darkening of the reaction mixture from pale yellow to a deep orange-red color, both forming the same photoproduct upon irradiation. Following the change by ^{1}H NMR spectroscopy, the clean formation of a new diamagnetic compound is observed that displays a complicated ^{1}H NMR spectrum indicative of molecular desymmetrization (Figure S7). This is best exemplified by the appearance of four singlets, each integrating to 9 protons, which are attributable to the individual *tert*-butyl groups of the aniline and ketimine moieties. Workup of the diamagnetic product into CH$_2$Cl$_2$ followed by diffusion with hexamethyldisiloxane gave single crystals which revealed the formation of the iron metallacycle product [κ^2-(^{t}Bu$_2$CN)C(η^6-NAr*)(*N*-NAr*)]Fe (**4**) (Scheme 1).

Scheme 1. Photolytic Synthesis of 1 and 4

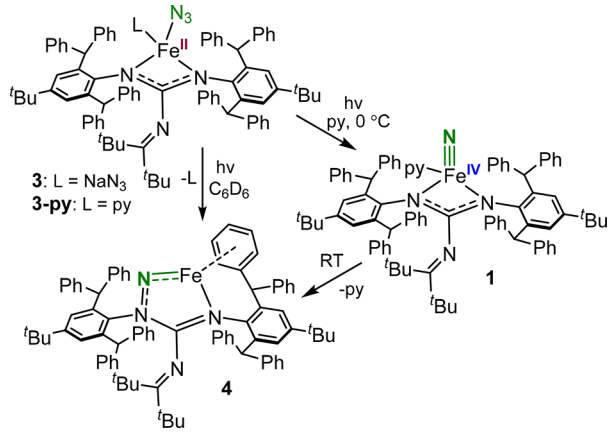

The solid-state structure of **4**·CH$_2$Cl$_2$ (Figure 3) shows a five-membered iron metallacycle formed via N$_2$ loss and ring

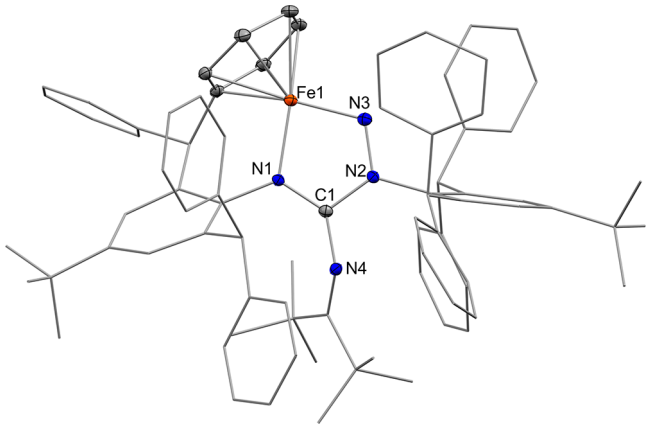

Figure 3. ORTEP diagram of **4**·CH$_2$Cl$_2$ with 30% thermal probability ellipsoids. Hydrogen atoms and co-crystallized molecule of CH$_2$Cl$_2$ omitted for clarity. Peripheral bonds de-emphasized for simplicity. Selected bond lengths (Å) and angles (deg): Fe1–N3 = 1.790(2), Fe1–N1 = 1.909(1), Fe1–N2 = 2.637(2), N2–N3 = 1.367(2), N1–C1 = 1.331(2), N2–C1 = 1.370(2), N4–C1 = 1.384(2), Fe–C$_{centroid}$ = 1.524, C$_{centroid}$–Fe1–N3 = 139.45, Fe1–N3–N2 = 112.6(1), N1–Fe1–N3 = 84.39(6).

expansion by N-atom insertion into an Fe–N^{Ar}* ligand bond. The resulting iron–nitrogen linkage exhibits an Fe1–N3 = 1.790(2) Å distance and a considerably bent Fe1–N3–N2 = 112.6(1)° bond angle. These metrical parameters suggest a bond order between that found for a typical single iron–nitrogen bond (cf. Fe[N(SiMe$_3$)$_2$]$_2$; Fe–N = 1.84 Å)[13] and those with formal Fe≡N–R bond character such as the Fe(II) imide complex {[PhB(CH$_2$PPh$_2$)$_3$]Fe≡NAd}$^-$ (Fe–N = 1.651(3) Å; Fe–N–C^{Ad} = 178.52(2)°) and the Fe(II) hydrazido (TPB)(CO)Fe≡N–N(SiMe$_2$CH$_2$)$_2$ (Fe–N = 1.6438(5); Fe–N–N = 160.37(5)°).[14] Accordingly, the Fe1–N3 bond in **4**·CH$_2$Cl$_2$ is comparable to that found in the Fe(II) iminyl radical complex (dipyrrin^{Ar})FeCl(•NC$_6$H$_4$-4-^{t}Bu) (Fe–N 1.768(2) Å; Fe–N–C = 156.4(2)°) which is described as possessing an attenuated iron-imido bond order.[15] The N2–N3 bond (1.367(2) Å) of **4**·CH$_2$Cl$_2$ is elongated in comparison to a diazene (ca. 1.25 Å)

DOI: 10.1021/jacs.7b06919
J. Am. Chem. Soc. 2017, 139, 15691–15700

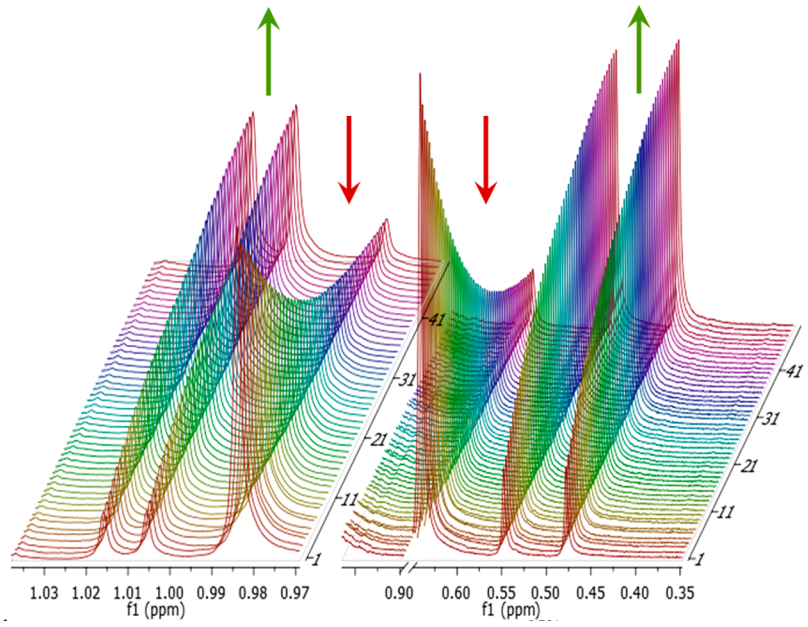

Figure 4. ^{1}H NMR spectral array of the conversion of $\mathbf{1}^{15N}$ to **4** in py-d_5 at room temperature collected at 15 min intervals.

but approximates the bond length found for metal hydrazidos (cf. Cp*Ti = $NNPh_2(Cl)(py)$, N−N = 1.386(3) Å).[16] Together with the inequivalent C1−N2 = 1.370(2) Å and C1−N1 = 1.331(2) Å distances of the guanidinate core, **4**·CH_2Cl_2 can be described as an Fe(II) hydrazido with partial Fe1−N3 double bond character. However, contributions from other resonance forms, e.g., Fe(0) diazenido, cannot be totally dismissed.[17]

Surprisingly, one of the aromatic rings from a pendant diphenylmethyl group is observed to form a close, masking interaction with the iron center (Fe−$C_{centroid}$ = 1.524 Å) of **4**·CH_2Cl_2, occupying the position of the displaced NaN_3 and py from **3-NaN$_3$** and **3-py**, respectively. Of note, this masking interaction is maintained in solution as evidenced by its NMR spectra in C_6D_6. For instance, the ^{1}H NMR spectrum of **4** shows five upfield shifted resonances from 4.61 to 5.67 ppm, each integrating to one proton, attributable to the hydrogens of the masking ring. Similarly, the corresponding carbon resonances appear in the ^{13}C NMR spectrum as six upfield shifted signals from 78.0 to 97.3 ppm.

Importantly, the conversion of **3** to **4** provides compelling evidence for the intermediate formation of an Fe(IV) nitride. As the ancillary ligand of **3**, namely NaN_3 or py, is evidently labile and ejected in this transformation, we suspected that its presence may play a critical role in the stabilization of the nitride intermediate. In an effort to trap it by providing an excess of coordinating base to favor the equilibrium toward a putative four-coordinate, coordinatively saturated intermediate, the photolysis of **3-py** in a dilute py-d_5 solution (ca. 1 mM) was performed at low temperature (0 °C). Pleasingly, this resulted in the near quantitative formation of a new, diamagnetic complex, formulated as **1** (Scheme 1), with approximate C_{2v} symmetry in solution as shown by ^{1}H, ^{13}C{^{1}H}, and ^{1}H−^{13}C HSQC NMR spectroscopies (Figures S9−S11). Complex **1** is stable for at least 24 h under the reaction conditions but gradually converts to **4** upon standing at room temperature over many hours (Figure 4). All attempts to isolate **1** in the solid-state failed owing to competitive conversion of the metastable iron nitride product to **4**. Additionally, use of excess hexamethylphosphoramide (HMPA) or 4-dimethylaminopyridine (DMAP) (ca. 20 equiv) as coordinating bases in benzene or pyridine solutions did not afford any discernible enhancement in the stability of **1**.

To further substantiate the identity of **1** as a bona fide Fe(IV)≡N complex, and aided by its diamagnetic character, ^{15}N NMR spectroscopic evidence was targeted as terminally bound iron nitrides give rise to signature resonances. The ^{15}N-labeled isotopomer $\mathbf{3}^{15N}$**-py** was synthesized using ^{15}N-isotopically enriched Na^{15}N═^{14}N═^{14}N. Photolysis of a ca. 10 mM solution of $\mathbf{3}^{15N}$**-py** in py-d_5 at 0 °C gives $\mathbf{1}^{15N}$ (50% Fe≡^{15}N) which displays a telltale resonance at 1016 ppm (vs externally referenced CH_3NO_2 at 380 ppm) in the ^{15}N NMR spectrum at −10 °C (Figure S12). This chemical shift is characteristic of late-metal terminal nitrides and in line with that found for **A** (952 ppm), **B** (1121 ppm), and **C** (1019 ppm).[2d,18]

Attempts to collect a ^{15}N NMR spectrum of the conversion product, $\mathbf{4}^{15N}$, for comparison failed due to a lack of a detectable signal. Regardless, the ^{15}N NMR signal for $\mathbf{4}^{15N}$ would be anticipated to appear significantly upfield from $\mathbf{1}^{15N}$ based upon the ^{15}N NMR spectrum for the Os(II) imide complex (η^6-C_6Me_6)OsN^tBu which is reported as a broad signal at 315 ppm (vs liquid NH_3 reference).[19] Alternatively, iron hydrazido complexes exhibit resonances that range from ca. −10 to 60 ppm (vs liquid NH_3).[20]

In addition to NMR spectroscopy, efforts were made to characterize **1** and $\mathbf{1}^{15N}$ via IR and Raman spectroscopies. The IR spectrum of **1**(KBr/pyridine) shows the clear disappearance of the band assigned to the azide stretch of **3-py** while exhibiting a few new peaks that sufficiently differentiate it from **4** (Figure S21). Unfortunately, assignment of bands attributable to the ν(Fe≡N) and ν(Fe≡^{15}N) vibrations of **1** and $\mathbf{1}^{15N}$, respectively, could not be made as the region in which these peaks would be expected to appear (~800−1100 cm^{-1})[4,6c] are obscured by strong ligand absorptions (Figure S22). Similarly, Raman analysis of a concentrated solution of **1** in pyridine was unsuccessful owing to the intense absorptions of the solvent.

Pleasingly, the photoconversion of **3-py** to **1** (Figure 5) and subsequently its transformation to **4** (Figure S14) can be tracked

DOI: 10.1021/jacs.7b06919
J. Am. Chem. Soc. 2017, 139, 15691−15700

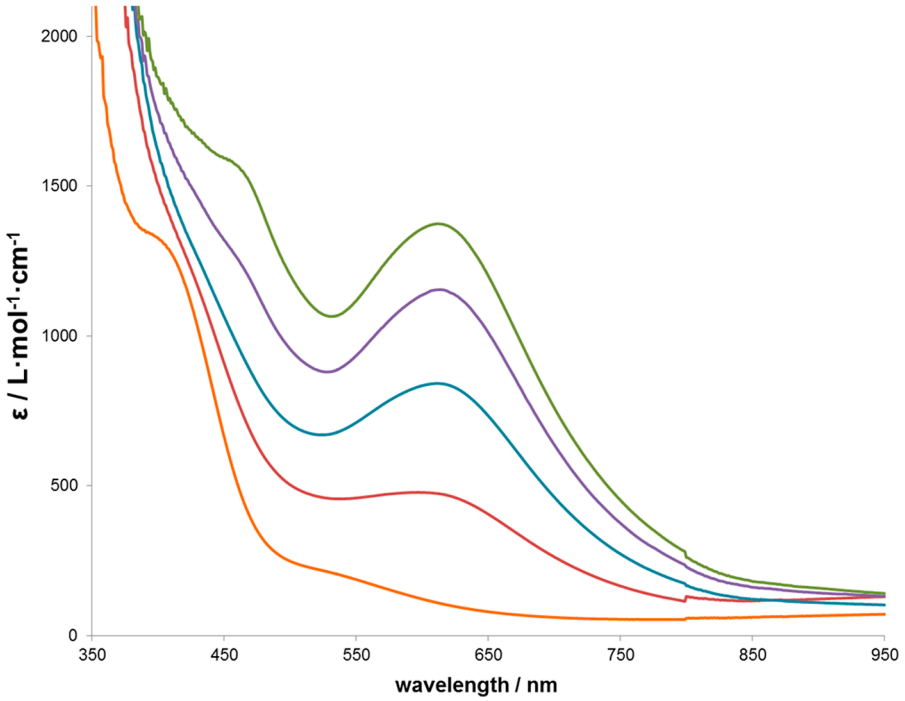

Figure 5. Electronic absorption spectra showing the photoconversion of **3-py** (1.4 mM; orange) in pyridine to **1** after 30 (red), 60 (blue), 90 (purple), and 120 (green) min of photolysis.

using electronic absorption spectroscopy as each of the complexes possesses a distinctive UV−vis absorption profile (Figure S13). For example, the formation of **1** in pyridine at 0 °C is shown in Figure 5 and is marked by the appearance of a prominent peak centered at 610 nm (ε = 1375 L·mol^{-1}·cm^{-1}), visually corresponding to a deep green solution color. In contrast, complexes **B** and **C** are described as orange-red and purple, respectively,[6a,c] while **A** is reported as tan in color.[4]

Computed Geometry and Electronic Structure. In the absence of a solid-state structure for **1**, given the sterics of the ligand, it is imaginable that the iron adopts either a three- or four-coordinate geometry. The formation of the former would be especially intriguing as, to the best of our knowledge, no three-coordinate metal nitrides are known. However, as **1** only persists in the presence of strongly coordinating pyridine, the latter scenario appears more likely. In order to provide further insights and to conclusively establish the geometry, electronic structure, and predict the reactivity of the nitride species **1**, computational analyses were performed using density functional theory (DFT) based methods. Namely, optimizations were carried out at the BLYP/def2-TZVP(-f) level of theory with electronic energies refined at TPSSh/def2-TZVP and solvent effect corrections determined using the SMD implicit solvation model as implemented in ORCA. The specifics of our computational protocol are detailed in the Supporting Information (SI).

The equilibrium structure of the full models of the three and four-coordinate derivatives of **1** were computed, additionally **4** was similarly modeled as a benchmark for which the computed geometry agrees reasonably well with the empirical XRD structure (Figure S27), substantiating the method of calculation. Furthermore, the computed ^{15}N NMR signal for **1** is found to be 1115 ppm which, when considering the error associated with computing chemical shielding, agrees reasonably well with the measured value of 1016 ppm. Finally, in line with experimental observations, the conversion of **1** to **4** is computed to be an energetically favorable process (ΔG_r = −3.0 kcal mol^{-1}) when evaluated at 0 °C using slightly truncated models, in which the *tert*-butyl groups of the aniline substituents were replaced by methyls. Using the same *in silico* methodology, we also modeled the molecular structures of **A**, **B**, and **C** and scrutinized their electronic structure in direct comparison to **1**.

Notably, the simulations reveal that the pyridine-bound, four-coordinate iron nitride species of **1** is more stable, by ∼10 kcal mol^{-1}, than the three-coordinate derivative (^{3}**1**) in which the pyridine ligand is excluded. Analysis of the respective spin states reveals a singlet ground state for **1**, in complete agreement with the diamagnetic character of its NMR spectra, while the only stable spin state found for the three-coordinate analog ^{3}**1** is a paramagnetic triplet with Fe(IV) centered, unpaired electrons. These data indicate that in contrast to the steric environment of the ligand, a preference for four-coordinate iron predominates in our system.

While we have no spectroscopic evidence for the formation of ^{3}**1**, the transition from **1** to ^{3}**1** is not energetically insurmountable, and it is conceivable that a small, yet undetectable, equilibrium amount of ^{3}**1** is present in solution. Indeed, in the transformation of **1** to **4**, three-coordinate ^{3}**1** may be the operative intermediate (vide infra), especially considering the necessity of lowered temperatures and pyridine as a coordinating solvent to stabilize **1**. Thus, the electronic structure and metrical parameters of ^{3}**1** warrant brief comment.

Interestingly, the iron center in ^{3}**1** (Figure S33) does not adopt a planar geometry, but instead can be described as exhibiting a distorted trigonal pyramidal geometry (N_{L1}−Fe−$N_{nitride}$ = 125.5°; N_{L2}−Fe−$N_{nitride}$ = 131.8°) with N^{Ar*}−Fe−$N_{nitride}$ bond angles that are only slightly larger than those calculated for **1** (vide infra). As may be expected with its higher spin state, the Fe−$N_{nitride}$ bond distance of 1.54 Å is slightly elongated as compared to **1** (Fe−$N_{nitride}$ = 1.517 Å) (Figure 6). These structural deformations in ^{3}**1**, with respect to four-coordinate **1**, are readily rationalized by its electronic structure as revealed by

DOI: 10.1021/jacs.7b06919
J. Am. Chem. Soc. 2017, 139, 15691−15700

using quasi-restricted orbitals (Figure S29). In **1**, the pyridine nitrogen atom points along a metal-based Fe≡N π*-orbital, and upon loss of the pyridine, this π*-orbital drops significantly in energy with additional stabilization achieved through dsp-hybridization. With this, the promotion of an electron from one of the δ-symmetry frontier d-orbitals to the deformed, but slightly still antibonding, Fe≡N π*-orbital becomes preferred over electron pairing, resulting in the triplet ground state of ^{3}**1**, the nonplanar geometry at iron, and the elongation of the Fe≡N bond.

From a conceptual point of view, the $N_{nitride}$ atom of ^{3}**1** possesses some radical character arising from the half-filled Fe≡N π*-orbital which we postulate is a major factor in the N-atom insertion process in the conversion of **1** to **4**. To quantify this, the spin densities at the $N_{nitride}$ and Fe atoms are found to be 0.16 a.u. and 1.74 a.u., respectively. For ^{3}**1**, we hypothesize that the π_2-orbital of the N−C−N moiety of the guanidinate ligand (N-centered with nodal plane at C) becomes the acceptor orbital upon the nitride insertion into the Fe−N_{L1} ligand bond. While the π_2-orbital of the anionic guanidinate ligand is occupied, its δ-symmetry aligns perfectly with the singly occupied, δ-symmetry d-orbital, allowing for ligand to metal donation as represented by HOMO−1 in Figure S30. As the insertion event proceeds, it can be imagined that π_2 to metal charge transfer occurs with the electron-density-shifting easing the coupling of the ligand nitrogen contact atom with the nitride center. A very similar N-migratory intramolecular insertion has been recently reported by Meyer and co-workers for a putative Co^{IV}≡N intermediate, also generated photochemically from the respective tripodal azido complex [(BIMPN^{Mes,Ad,Me})$Co^{II}(N_3)$].[21] In [(BIMPN^{Mes,Ad,Me})Co≡N], the empty π*-orbital of the carbene ligand plays the role of the electron acceptor upon intramolecular N-migratory insertion.[21] In line with their experimental observations, an extremely facile (activation barrier 2.2 kcal mol^{-1}) N-insertion into a Co−$C_{carbene}$ bond was calculated yielding, after a spin transition from the doublet to the quartet surface and an H-atom abstraction event, an imine complex.

The computed structure of four-coordinate **1** (Figure 6) depicts an approximately tetrahedral complex. The τ_4 parameter, a four coordinate geometry index, of **1** is τ_4 = 0.72, indicative of a distorted tetrahedral geometry.[22] For comparison, the τ_4 values of **B** and **C** show slightly more idealized tetrahedral structures with τ_4 = 0.83 and 0.81, respectively. In **1**, the iron is observed to sit ca. 0.8 Å out of the plane defined by the ligating guanidinate and pyridine nitrogen atoms. This displacement falls between that reported for **B** (ca. 1 Å) and **C** (ca. 0.4 Å).[6a] The most salient feature of **1**, its Fe−$N_{nitride}$ bond, is found at a distance of 1.517 Å. This bond length is short and consistent with an Fe(IV) center with a triply bonded terminal nitride, in excellent agreement with experimentally determined Fe≡N distances of 1.51−1.55 Å reported for **A**−**C**.[5,6,6c] Inspection of the Fe≡N interaction in **1** reveals strong mixing of the π-type Fe($d_{xz,yz}$) and N($p_{x,y}$) atomic orbitals (e.g., π_2 in Figure 7 consists of 20% Fe and 29% of $N_{nitride}$ contribution) that signals a significant degree of covalent character in the iron nitride bond, reminiscent of the orbital mixing found in **A**−**C**. The notion of a strongly covalent iron nitride bond is further supported by the Mayer bond order of 2.53 computed for the Fe≡N moiety of **1**.

Inspection of the frontier orbital ordering in **1**, shown in Figure 7, is particularly revealing. The formal electronic ground state configuration of $(d_{xy})^2(d_{x^2-y^2})^2(d_{xz})^0(d_{yz})^0(d_{z^2})^0$ is in accordance with a low-spin Fe(IV) complex possessing a nearly degenerate LUMO and LUMO+1 of predominantly Fe($d_{xz,yz}$)N($p_{x,y}$)

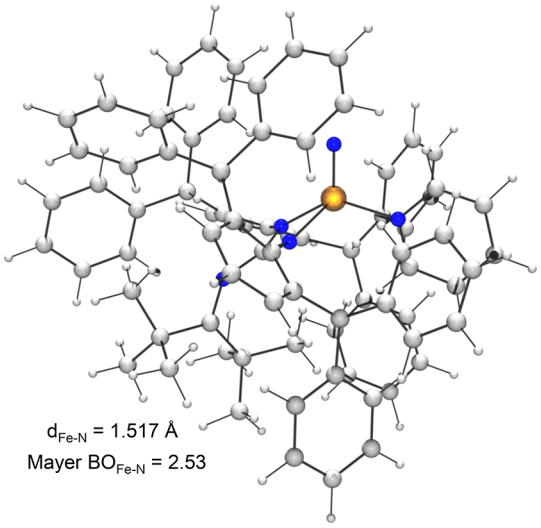

Figure 6. Computed equilibrium structure of **1**. Selected calculated bond distances (Å) and angles (deg): Fe−$N_{nitride}$ = 1.517, Fe−N_{L1} = 2.009, Fe−N_{L2} = 1.997, Fe−N_{py} = 1.889, N_{L1}−Fe−$N_{nitride}$ = 127.7, N_{L2}−Fe−$N_{nitride}$ = 112.3, N_{py}−Fe−$N_{nitride}$ = 107.5, N_{py}−Fe−N_{L1} = 108.6, N_{L1}−Fe−N_{L2} = 67.4, N_{L2}−Fe−N_{py} = 130.6.

π*-character. Significantly, this splitting pattern differs markedly from the $(d_{xy})^2(d_{x^2-y^2})^2(d_{z^2})^0(d_{xz})^0(d_{yz})^0$ ordering found for **A**−**C**, wherein the LUMO is comprised by the Fe(d_{z^2})N(p_z) σ*-orbital. This phenomenon in **A**−**C** is unexpected as the very short Fe≡N distances in these complexes are suggestive of a strong iron-nitride σ-bond, which should be reflected by a high-lying σ*-orbital. The unusual bond ordering in **A**−**C** is typically explained by invoking $3d_{z^2}$/4s/4p_z mixing at iron which decreases the Fe(d_{z^2})N(p_z) σ-bond overlap, that together with the beneficial orientation of σ-donor ligands results in a low-energy reciprocal σ*-component.[2d] Interestingly, this does not appear to be the case in **1** as its Fe(d_{z^2})N(p_z) σ*-bond is found higher in relative energy (LUMO+3) than its Fe≡N π*-antibonding orbitals (LUMO, LUMO+1), signaling a significant Fe(d_{z^2})N(p_z) overlap and a strong Fe≡N σ-interaction (Figure 7, Figure S28).

Given that **1** and **A**−**C** share similar geometric indices at iron, their electronic differences may be reconciled in terms of comparative ligand field contributions. In contrast to the strong-field character of the ligands in **A**−**C**, the weaker σ-donor ability of the guanidinate ligand in **1** could in principle give rise to the observed disparity between the Fe≡N orbital orderings in **1** and **A**−**C**, which in turn may be framed in terms of relative σ-donor contributions. While guanidinates are considered competent electron donors,[10a,b] studies have shown they are far exceeded in donor strength by bidentante, bis(carbenes) and, by extension, tripodal, tris(carbene), and tris(phosphine) ligands such as those found in **A**−**C**.[23] We posit that as a result of the exceptional σ-donor abilities of the phosphine and NHC ligands in **A**−**C**, the d_{z^2} undergoes the reported hybridization to minimize the overlap with the lone pairs of these ligands. Without this $3d_{z^2}$/4s/4p_z mixing, we hypothesize the σ-electron density at iron would be much more significant and would exert a considerable Pauli repulsion toward the nitride's filled N(p_z) orbital, which would result in a longer and weaker Fe≡N interaction. As a consequence, the resulting $3d_{z^2}$/4s/4p_z hybrid orbital leads to a reduced net overlap in the σ-component of the iron-nitride bond,[6a] while the Fe−N distance remains short, which is advantageous for the iron-nitride Fe($d_{xz,yz}$)N($p_{x,y}$) π-bonding and electrostatic interactions.

DOI: 10.1021/jacs.7b06919
J. Am. Chem. Soc. 2017, 139, 15691−15700

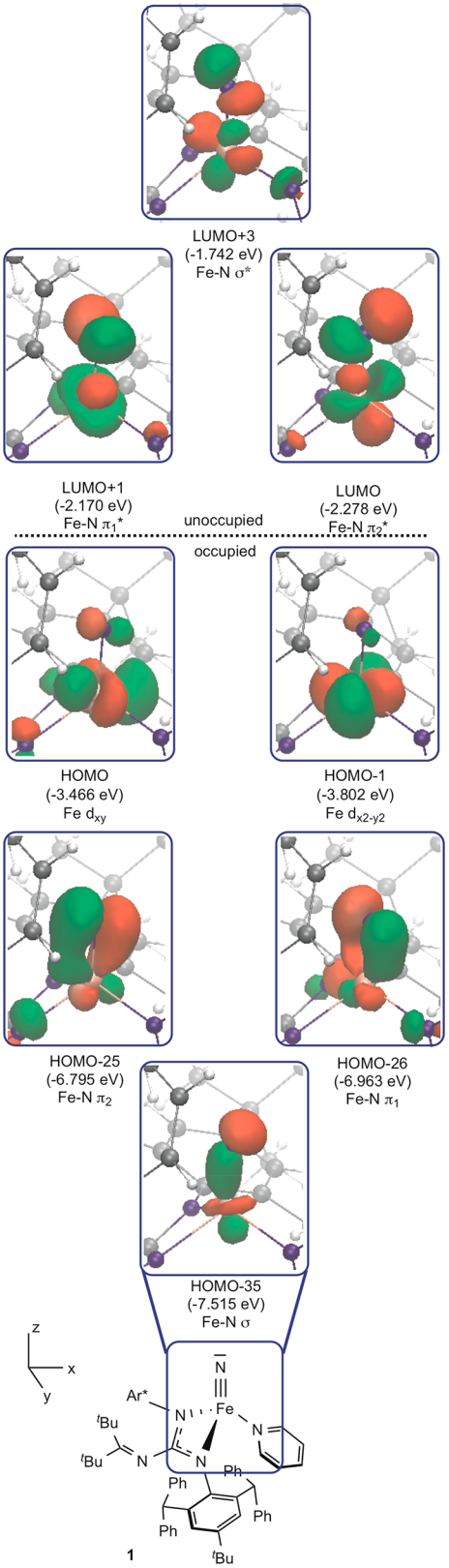

Figure 7. Molecular orbital diagram representing the Fe≡N bonding in **1**.

In contrast, due to the comparatively reduced σ-donor ability of the guanidinate, the iron center in **1** is electron deficient with respect to **A**–**C**. Accordingly, there is no such electronic constraint on its $3d_{z^2}$ orbital, allowing a "classical" strong σ-interaction with the N(p_z) orbital. Mulliken (and [Löwdin]) atomic charges of the Fe and $N_{nitride}$ atoms clearly support the notion of an electron-rich iron in **A** (q_{Fe} = 0.0 *e*, q_N = −0.3 *e*) [q_{Fe} = −0.6 *e*, q_N = 0.0 *e*], **B** (q_{Fe} = 0.1 *e*, q_N = −0.4 *e*) [q_{Fe} = −0.3 *e*, q_N = −0.1 *e*], and **C** (q_{Fe} = 0.2 *e*, q_N = −0.2 *e*) [q_{Fe} = −0.3 *e*, q_N = 0.0 *e*], whereas a more electron-deficient iron center appears in **1** (q_{Fe} = 0.5 *e*, q_N = −0.6 *e*) [q_{Fe} = −0.2 *e*, q_N = 0.0 *e*]. Also, while our calculations indeed reproduce the earlier reported dsp-type hybridization at iron for the Fe≡N σ-interaction in **A** (the d:s:p(Fe) shell contributions are 19:6:0 in percentages in the total σ-bond), **B** (21:1:1), and **C** (29:3:2), this hybridization is completely absent in the dominant σ-type MO of **1** (HOMO−35 in Figure 7). In line with this reasoning, the Fe≡N type σ–σ* splitting is larger in **1** (5.8 eV) than in **A** (5.2 eV), **B** (5.3 eV), and **C** (5.5 eV).

The σ-donor ability of the supporting ligand(s) also has a direct, two-fold effect on the Fe≡N π-bonding. First, due to simple electrostatics, the metal-centered orbitals are higher in energy at an electron-rich iron, like in **A**-**C**, than in **1**, which is supported by weaker σ-donors. More importantly, in an ideal tetrahedral arrangement, the π-type acceptor d-orbitals (the t_2 set) are antibonding with respect to the σ-interactions;[24] i.e., strong σ-donors elevate the π-type acceptor d-orbitals more than weak σ-donors do. We contend that in **A**–**C** these effects lead to a better energy match of the iron d_{xz} and d_{yz} π-acceptor orbitals with the p_x and p_y π-donor orbitals of the $N_{nitride}$ atom, resulting in stronger π-type Fe≡N interactions which is manifested through increased π–π* splitting in **A** (5.6 eV), **B** (5.3 eV), and **C** (5.6 eV) as compared to that in **1** (4.6 eV). Additionally, the relative atomic contributions to the corresponding MOs imply more covalent interactions in the former set. All combined, for **1**, these effects lead to a decreased HOMO–LUMO gap (~1.2 eV) and "reversed" ordering of Fe–$N_{nitride}$ σ* and π* orbitals in **1** in relation to **A**–**C** (HOMO–LUMO gaps between ~1.6 and 1.9 eV.)

This analysis is further corroborated by the electronic absorption spectra of **1** which displays a pronounced absorption feature at 610 nm (ε = 1375 L·mol^{-1}·cm^{-1}), bathochromically shifted from those reported for **B** (477 nm, ε = 1230 L·mol^{-1}·cm^{-1}; 324 nm, ε = 7292 L·mol^{-1}·cm^{-1}; 264 nm, ε = 8708 L·mol^{-1}·cm^{-1}) and **C** (520 nm, ε = 1980 L·mol^{-1}·cm^{-1}).[6a,c] To probe the nature of the 610 nm absorption feature in **1**, TD-DFT at TPSSh/def2-TZVP calculations (see further details in SI) reveals a high probability excitation transition at 613 nm with $d_{x^2-y^2}$-to-π_y* character. This nicely corresponds to the HOMO−1 to LUMO+1 (Figure 7) electronic transition upon photoabsorption.

Finally, while we posit that ligand field effects exert a significant influence over the respective $3d_{z^2}$ ordering and hybridization energies of **1** and **A**–**C**, molecular symmetry effects must also be considered. As compared to the approximate C_3v symmetries of **A**–**C**, complex **1** possesses a reduced pseudo C_2v symmetry. This permits increased orbital mixing, even in the σ and π-subspaces and corresponding d-orbitals, that is observable for example in the form of the LUMO, LUMO+1, and LUMO+3 of **1** in Figure 7. Judging from the 0.1 eV separations of the π_x* and π_y*, as well as π_x and π_y orbitals which are perfectly degenerate in **A**–**C**, the stabilizing effect of symmetry breaking in **1** appears as a minor contributor in the role of spatial distribution and relative stability of the d-orbital ordering energies.

Reactivity. Complexes containing terminal metal-nitride functionalities have been shown useful as N-atom transfer vehicles.[25] However, the reaction scope of molecular iron-nitrides and their potential for N-atom transfer has been limited to studies with **A** and **B** with only the latter examined to a

DOI: 10.1021/jacs.7b06919
J. Am. Chem. Soc. 2017, 139, 15691−15700

significant extent.[2d,4,26] Fortunately, the solution stability of **1** allows us access to probe its chemistries, and a preliminary investigation into its reactivity has been conducted.

Treatment of **1** with PMe_2Ph instantaneously gives the paramagnetic Fe(II) phosphiniminate $[L^{Ar*}]Fe(N{=}PMe_2Ph)(py)$ (**5**), which can be isolated as a dark orange solid (Scheme 2).

Scheme 2. N-Atom-Transfer Reactivity of 1

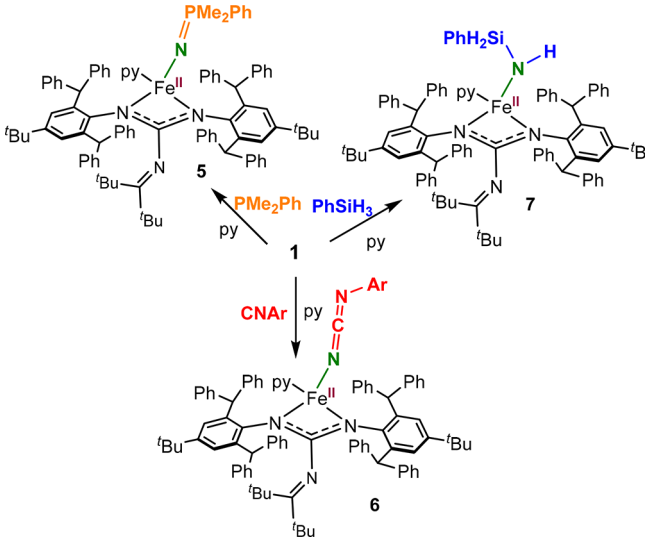

Complex **3-py** does not react with PMe_2Ph in the absence of UV irradiation, but **5** can be synthesized by photolysis of **3-py** solution in the presence of excess PMe_2Ph. This seemingly mirrors the chemistry of **A** and **B** with tertiary phosphines, which gives $[PhB(CH_2P^iPr_2)_3]Fe{-}N{=}PR_3$ and $[PhB(^{tBu}Im)_3]Fe{-}N{=}PR_3$, respectively.[2d,4] Yet, based on the orbital ordering calculated for **1**, nucleophilic addition by the phosphine would be expected to happen at a low-lying $Fe(d_{xz,yz})N(p_{x,y})$ π^*-orbital, versus at the $Fe(d_{z2})N(p_z)$ σ^*-orbitals of **A** and **B**, suggesting that phosphine attack would occur at an angle relative to the Fe≡N vector rather than via an end-on approach. To support this notion, the transition state for the reaction between a truncated version of **1** (**1′**) and PMe_3 was calculated. As shown in Figure S31, the reaction profile reveals a transition state, **1′**-TS, with an $Fe{-}N_{nitride}{-}P$ approach angle of ca. 147° consistent with attack at an Fe≡N π^*-orbital. This stands in contrast to the more linear $Fe{-}N_{nitride}{-}P$ (162°) transition-state geometry calculated for an abridged model of **B** with PH_3.[26b] Moreover, one of the valence MOs (Figure S32) clearly features the expected overlap of the nucleophile's lone-pair and one of the Fe−N π^*-orbitals. Though, an interesting feature of the simulated transition state is the slight distortion of the geometry at the phosphorus atom of PMe_3 from tetrahedral toward a saw-horse geometry. This implies that the lone-pair of the nitride also develops an orbital interaction with the phosphorus center. This can be intuitively rationalized through nucleophilicity enhancement of the nitride as the PMe_3 donates electrons to the Fe≡N π^* orbital, concomitantly resulting in a N=P double bond in **5**.

Similarly, addition of ArN≡C (Ar = 2,6-dimethylphenyl) to **1** results in partial N-atom transfer, generating the paramagnetic carbodiiminate $[L^{Ar*}]Fe(N{=}C{=}NAr)(py)$ (**6**) as a pale yellow solid (Scheme 2), akin to the reactivity reported for **B** with ^{t}BuNC which gives $[PhB(^{tBu}Im)_3]Fe{-}N{=}CN^tBu$.[2d] Complex **6** can also be synthesized in situ by photolyzing a pyridine mixture of **3-py** with excess ArNC.

Monitoring the reactions of **1** with PMe_2Ph and ArNC by NMR spectroscopy reveals quantitative conversion to the paramagnetic products **5** and **6**; however, isolated yields of 30% and 38%, respectively, are lower owing to the solubility of the materials under the conditions of crystallization. The identity of the products was confirmed by spectroscopic methods, elemental analysis, and X-ray structural determination (see SI).

To test the competency of **1** as a model for N_2 fixation, as in the Haber−Bosch process, its reactivity with hydrogen sources was examined. Photolysis of **3-py** in py-d_5 at room temperature under ~100 psi H_2 resulted exclusively in the formation of **4**. Similarly, no reaction was observed between **1** and cyclohexadiene. However, irradiation of **3-py** in the presence of the H_2 substitute $PhSiH_3$ generates the Fe(II) amide complex $[L^{Ar*}]Fe[N(H)(SiH_2Ph)](py)$ (**7**) via N-atom insertion into the Si−H bond (Scheme 2), and its solid-state structure is shown in Figure 8.

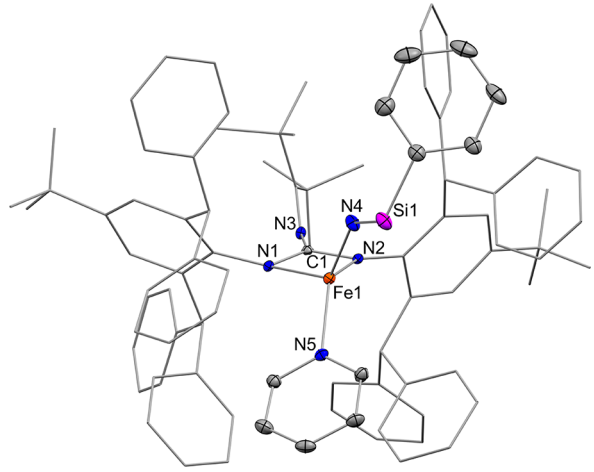

Figure 8. ORTEP diagram of $7{\cdot}2Et_2O$ with 30% thermal probability ellipsoids. Hydrogen atoms and co-crystallized Et_2O molecules are omitted for clarity. Peripheral bonds de-emphasized for simplicity. Selected bond lengths (Å) and angles (deg): Fe1−N1 = 2.129(7), Fe1−N2 = 2.068(2), Fe1−N4 = 1.948(7), Fe1−N5 = 2.068(5), Fe1−N4−Si1 = 137.2(7).

Notably, the reactivity of iron nitrides with silanes has not been reported but is akin to that known for other late-metal nitrides.[27] Complex **7** is paramagnetic and isolated as a yellow, crystalline solid in 39% yield. Interestingly, **7** is thermally unstable and slowly converts to a new, as of yet unidentified, paramagnetic compound in solution at room temperature. Efforts to isolate and characterize this secondary product are underway.

While the reactivity of **1** with phosphines and isocyanides can be framed in the context of its electronic structure, i.e., accessible low-lying vacant π^*-orbitals, explaining the reactivity of **1** with $PhSiH_3$ is, however, not as straightforward. It is conceivable that the reaction might proceed either through a concerted, electrophilic insertion of the nitride into the Si−H bond or via nucleophilic attack of the nitride on silicon, followed by a hydride shift. To gain a first insight into this dilemma, we further scrutinized the intrinsic reactivity of the Fe≡N functionality by computing the nucleophilic and electrophilic Fukui functions, f^+ and f^-, of **1** (Figure 9) using the finite difference approach. These real-space reactivity measures intuitively reveal the most electrophilic and nucleophilic centers/regions of **1**, respectively, by indicating an electron accumulation (f^+) at the nitride center (i.e., electrophilic reactivity at the nitride) and a dominantly metal-centered electron

DOI: 10.1021/jacs.7b06919
J. Am. Chem. Soc. 2017, 139, 15691−15700

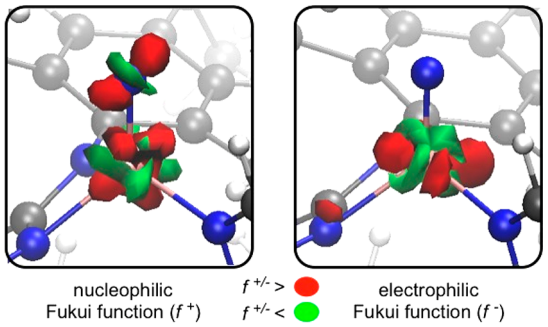

Figure 9. Fukui function f^+ and f^- of **1** showing the sites of nucleophilic and electrophilic attack, respectively.

depletion (f^-) process (i.e., nucleophilic reactivity is predicted at iron). Under this working model, the data support direct electrophilic insertion of the nitride center into the Si−H bond in the reaction of **1** with $PhSiH_3$, which is highly plausible given its reactivity patterns with nucleophiles. Nonetheless, the possibility of H-atom abstraction by ^{3}**1**, as an excited-state species, followed by rebound of the resulting silyl radical, cannot be discounted at this time, and future studies are planned to reconcile this.

SUMMARY

Using the super bulky guanidinate $[L^{Ar*}]^-$ (L^{Ar*} = $(Ar*N)_2C(R)$, Ar* = 2,6-bis(diphenylmethyl)-4-*tert*-butylphenyl, R = NC^tBu_2) for kinetic stabilization, photolysis of $[L^{Ar*}]FeN_3(py)$ (**3-py**) at 0 °C in pyridine generates the diamagnetic, terminal iron nitride $[L^{Ar*}]FeN(py)$ (**1**) which was characterized by solution-state NMR and electronic absorption spectroscopies. Computational modeling of **1** supports a four-coordinate, pseudo-tetrahedral complex where pyridine acts as an auxiliary ligand. Interestingly, calculations show that the three-coordinate, paramagnetic triplet $[L^{Ar*}]FeN$ (^{3}**1**), which sits approximately 10 kcal/mol higher in energy, is a potentially accessible excited state; however, its presence was not detected.

Notably, though, the computations and the UV−vis absorption profile reveal a Fe≡N electronic structure in **1** that is characteristically distinct from the isolable four-coordinate Fe(IV) nitrides $[PhB(CH_2P^iPr_2)_3]Fe^{IV}{\equiv}N$ (**A**), $[PhB(^{tBu}Im)_3]Fe^{IV}{\equiv}N$ (**B**), and $[(TIMEN^R)Fe^{IV}{\equiv}N]^+$ (**C**). In particular, calculations indicate in **1** a different frontier orbital ordering that features a shallower HOMO−LUMO gap, which we attribute to the weaker ligand field contributions of the guanidinate ligand and, to a smaller extent, orbital mixing effects from its comparatively lower molecular symmetry.

In contrast to **A**−**C**, complex **1** is metastable, giving rise to intramolecular N-atom insertion to generate the Fe(II) hydrazide complex $[\kappa^2$-$(^tBu_2CN)C(\eta^6$-$NAr*)(N$-$NAr*)]Fe$ (**4**) upon standing at room temperature. Partial N-atom transfer is also observed upon addition of PMe_2Ph and ArN≡C (Ar = 2,6-dimethylphenyl) to **1**, yielding the Fe(II) products $[L^{Ar*}]Fe(N{=}PMe_2Ph)(py)$ (**5**) and $[L^{Ar*}]Fe(N{=}C{=}NAr)(py)$ (**6**), respectively. Interestingly, **1** also reacts with the H_2 stand-in $PhSiH_3$ to give $[L^{Ar*}]Fe[N(H)(SiH_2Ph)](py)$ (**7**) via a proposed electrophilic N-atom insertion pathway into the Si−H bond. Currently, we are further exploring the chemistry of **1** with other substrates while investigating the impact of ligand modifications on the Fe≡N functionality to further test structure−function relationships and ligand field effects on its electronic structure.

ASSOCIATED CONTENT

Supporting Information

The Supporting Information is available free of charge on the ACS Publications Web site. Crystallographic details (CIF) The Supporting Information is available free of charge on the ACS Publications website at DOI: 10.1021/jacs.7b06919.

Experimental procedures, spectral data for all complexes, and computational details. (PDF)
Crystallographic details (CIF)
Crystallographic details (CIF)
Crystallographic details (CIF)
Crystallographic details (CIF)
Crystallographic details (CIF)
Crystallographic details (CIF)

AUTHOR INFORMATION

Corresponding Authors

*asfortier@utep.edu
*pbalazs@vub.ac.be

ORCID

Balazs Pinter: 0000-0002-0051-5229
Skye Fortier: 0000-0002-0502-5229

Notes

The authors declare no competing financial interest.

ACKNOWLEDGMENTS

We are grateful to the University of Texas at El Paso, NSF PREM Program (DMR-1205302), and the NSF (CHE-1664938; S.F) for financial support of this work. B.P. thanks the Research Foundation − Flanders (FWO) for the continuous financial support.

REFERENCES

(1) Ertl, G. *Angew. Chem., Int. Ed. Engl.* **1990**, *29*, 1219−1227.
(2) (a) Hoffman, B. M.; Dean, D. R.; Seefeldt, L. C. *Acc. Chem. Res.* **2009**, *42*, 609−619. (b) Hoffman, B. M.; Lukoyanov, D.; Yang, Z. Y.; Dean, D. R.; Seefeldt, L. C. *Chem. Rev.* **2014**, *114*, 4041−4062. (c) Seefeldt, L. C.; Hoffman, B. M.; Dean, D. R. *Annu. Rev. Biochem.* **2009**, *78*, 701−722. (d) Smith, J. M.; Subedi, D. *Dalton Trans.* **2012**, *41*, 1423−1429. (e) Hohenberger, J.; Ray, K.; Meyer, K. *Nat. Commun.* **2012**, *3*, 720.
(3) McDonald, A. R.; Que, L., Jr. *Coord. Chem. Rev.* **2013**, *257*, 414−428.
(4) Betley, T. A.; Peters, J. C. *J. Am. Chem. Soc.* **2004**, *126*, 6252−6254.
(5) Rohde, J. U.; Betley, T. A.; Jackson, T. A.; Saouma, C. T.; Peters, J. C.; Que, L. *Inorg. Chem.* **2007**, *46*, 5720−5726.
(6) (a) Scepaniak, J. J.; Fulton, M. D.; Bontchev, R. P.; Duesler, E. N.; Kirk, M. L.; Smith, J. M. *J. Am. Chem. Soc.* **2008**, *130*, 10515−10517. (b) Scepaniak, J. J.; Vogel, C. S.; Khusniyarov, M. M.; Heinemann, F. W.; Meyer, K.; Smith, J. M. *Science* **2011**, *331*, 1049−1052. (c) Vogel, C.; Heinemann, F. W.; Sutter, J.; Anthon, C.; Meyer, K. *Angew. Chem., Int. Ed.* **2008**, *47*, 2681−2684.
(7) (a) Rodriguez, M. M.; Bill, E.; Brennessel, W. W.; Holland, P. L. *Science* **2011**, *334*, 780−783. (b) MacLeod, K. C.; Menges, F. S.; McWilliams, S. F.; Craig, S. M.; Mercado, B. Q.; Johnson, M. A.; Holland, P. L. *J. Am. Chem. Soc.* **2016**, *138*, 11185−11191.
(8) (a) Wagner, W. D.; Nakamoto, K. *J. Am. Chem. Soc.* **1988**, *110*, 4044−4045. (b) Wagner, W. D.; Nakamoto, K. *J. Am. Chem. Soc.* **1989**, *111*, 1590−1598. (c) Aliaga-Alcalde, N.; George, S. D.; Mienert, B.; Bill, E.; Wieghardt, K.; Neese, F. *Angew. Chem., Int. Ed.* **2005**, *44*, 2908−2912. (d) Meyer, K.; Bill, E.; Mienert, B.; Weyhermuller, T.; Wieghardt, K. *J. Am. Chem. Soc.* **1999**, *121*, 4859−4876. (e) Grapperhaus, C. A.; Mienert, B.; Bill, E.; Weyhermuller, T.; Wieghardt, K. *Inorg. Chem.* **2000**, *39*, 5306−5317. (f) Berry, J. F.; Bill, E.; Bothe, E.; George, S. D.; Mienert, B.; Neese, F.; Wieghardt, K. *Science* **2006**, *312*, 1937−1941.

DOI: 10.1021/jacs.7b06919
J. Am. Chem. Soc. 2017, 139, 15691−15700

(g) Schlangen, M.; Neugebauer, J.; Reiher, M.; Schröder, D.; López, J. P.; Haryono, M.; Heinemann, F. W.; Grohmann, A.; Schwarz, H. *J. Am. Chem. Soc.* **2008**, *130*, 4285−4294.
(9) Maity, A. K.; Fortier, S.; Griego, L.; Metta-Magaña, A. J. *Inorg. Chem.* **2014**, *53*, 8155−8164.
(10) (a) Castillo, M.; Barreda, O.; Maity, A. K.; Barraza, B.; Lu, J.; Metta-Magana, A. J.; Fortier, S. *J. Coord. Chem.* **2016**, *69*, 2003−2014. (b) Maity, A. K.; Metta-Magaña, A. J.; Fortier, S. *Inorg. Chem.* **2015**, *54*, 10030−10041. (c) Eckert, N. A.; Smith, J. M.; Lachicotte, R. J.; Holland, P. L. *Inorg. Chem.* **2004**, *43*, 3306−3321. (d) Cowley, R. E.; Holland, P. L. *Inorg. Chem.* **2012**, *51*, 8352−8361.
(11) Buschhorn, D.; Pink, M.; Fan, H.; Caulton, K. G. *Inorg. Chem.* **2008**, *47*, 5129−5135.
(12) (a) Tornieporth-Oetting, I. C.; Klapotke, T. M. *Angew. Chem., Int. Ed. Engl.* **1995**, *34*, 511−520. (b) Haiges, R.; Boatz, J. A.; Yousufuddin, M.; Christe, K. O. *Angew. Chem., Int. Ed.* **2007**, *46*, 2869−2874.
(13) Andersen, R. A.; Faegri, K.; Green, J. C.; Haaland, A.; Lappert, M. F.; Leung, W. P.; Rypdal, K. *Inorg. Chem.* **1988**, *27*, 1782−1786.
(14) (a) Brown, S. D.; Peters, J. C. *J. Am. Chem. Soc.* **2005**, *127*, 1913−1923. (b) Moret, M. E.; Peters, J. C. *J. Am. Chem. Soc.* **2011**, *133*, 18118−18121.
(15) King, E. R.; Hennessy, E. T.; Betley, T. A. *J. Am. Chem. Soc.* **2011**, *133*, 4917−4923.
(16) (a) Allen, F. H.; Kennard, O.; Watson, D. G.; Brammer, L.; Orpen, A. G.; Taylor, R. *J. Chem. Soc., Perkin Trans. 2* **1987**, S1−S19. (b) Selby, J. D.; Feliz, M.; Schwarz, A. D.; Mountford, P. *Organometallics* **2011**, *30*, 2295−2307.
(17) Müller, A. L.; Bleith, T.; Roth, T.; Wadepohl, H.; Gade, L. H. *Organometallics* **2015**, *34*, 2326−2342.
(18) (a) Scheibel, M. G.; Askevold, B.; Heinemann, F. W.; Reijerse, E. J.; de Bruin, B.; Schneider, S. *Nat. Chem.* **2012**, *4*, 552−558. (b) Schoffel, J.; Rogachev, A. Y.; George, S. D.; Burger, P. *Angew. Chem., Int. Ed.* **2009**, *48*, 4734−4738. (c) Walstrom, A.; Pink, M.; Yang, X.; Tomaszewski, J.; Baik, M.-H.; Caulton, K. G. *J. Am. Chem. Soc.* **2005**, *127*, 5330−5331.
(19) Michelman, R. I.; Bergman, R. G.; Andersen, R. A. *Organometallics* **1993**, *12*, 2741−2751.
(20) Saouma, C. T.; Lu, C. C.; Peters, J. C. *Inorg. Chem.* **2012**, *51*, 10043−10054.
(21) Zolnhofer, E. M.; Käß, M.; Khusniyarov, M. M.; Heinemann, F. W.; Maron, L.; van Gastel, M.; Bill, E.; Meyer, K. *J. Am. Chem. Soc.* **2014**, *136*, 15072−15078.
(22) Yang, L.; Powell, D. R.; Houser, R. P. *Dalton Trans.* **2007**, 955−964.
(23) (a) Hickey, A. K.; Lee, W. T.; Chen, C. H.; Pink, M.; Smith, J. M. *Organometallics* **2016**, *35*, 3069−3073. (b) Munoz, S. B.; Foster, W. K.; Lin, H. J.; Margarit, C. G.; Dickie, D. A.; Smith, J. M. *Inorg. Chem.* **2012**, *51*, 12660−12668. (c) Kelley, M. R.; Rohde, J. U. *Inorg. Chem.* **2013**, *52*, 2564−2580. (d) Smith, J. *Comments Inorg. Chem.* **2008**, *29*, 189−233.
(24) Albright, T. A.; Burdett, J. K.; Whangbo, M. H. *Orbital Interactions in Chemistry*; Wiley: New York, 1985.
(25) (a) Du Bois, J.; Tomooka, C. S.; Hong, J.; Carreira, E. M. *Acc. Chem. Res.* **1997**, *30*, 364−372. (b) Klopsch, I.; Kinauer, M.; Finger, M.; Wurtele, C.; Schneider, S. *Angew. Chem., Int. Ed.* **2016**, *55*, 4786−4789. (c) Ishida, Y.; Kawaguchi, H. *J. Am. Chem. Soc.* **2014**, *136*, 16990−16993. (d) Clarke, R. M.; Storr, T. *J. Am. Chem. Soc.* **2016**, *138*, 15299−15302. (e) Keener, M.; Peterson, M.; Hernández Sánchez, R.; Oswald, V. F.; Wu , G.; Ménard, G. *Chem. Eur. J.* **2017**, *48*, 11479−11484.
(26) (a) Lee, W.-T.; Juarez, R. A.; Scepaniak, J. J.; Muñoz, S. B.; Dickie, D. A.; Wang, H.; Smith, J. M. *Inorg. Chem.* **2014**, *53*, 8425−8430. (b) Scepaniak, J. J.; Margarit, C. G.; Harvey, J. N.; Smith, J. M. *Inorg. Chem.* **2011**, *50*, 9508−9517. (c) Scepaniak, J. J.; Bontchev, R. P.; Johnson, D. L.; Smith, J. M. *Angew. Chem., Int. Ed.* **2011**, *50*, 6630−6633.
(27) Sieh, D.; Schoffel, J.; Burger, P. *Dalton Trans.* **2011**, *40*, 9512−9524.

DOI: 10.1021/jacs.7b06919
J. Am. Chem. Soc. 2017, 139, 15691−15700